



Cite this: *J. Mater. Chem. C*, 2017, 5, 12338

Received 21st September 2017,
Accepted 30th October 2017

DOI: 10.1039/c7tc04316c

rsc.li/materials-c

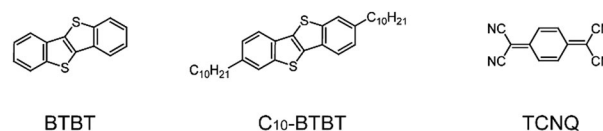
Here, using solution based self-assembly, we contrast a three-dimensional co-crystal, where a [1]benzothieno[3,2-*b*][1]benzothiophene (BTBT) based donor and a tetracyanoquinodimethane (TCNQ) based acceptor leads to a mixed stacking sequence with pronounced intermolecular hybridization, with the donor–acceptor bilayer. Despite a comparable increase in conductivity, we observe a co-crystal with unique mechano-pyro-electric coupling properties.

Introduction

A key characteristic of molecular charge-transfer electronics is their solid crystalline structure resulting in the presence of multidimensional interfaces that have a great impact on their electronic performance.¹ Given the success of organic semiconductors in practical applications,² the fundamental charge-transfer processes in molecular donor–acceptor complexes have been elusive. Thus, a detailed understanding of the processes taking place between molecular donor and acceptor building blocks is of crucial importance. Depending on their molecular arrangement and charge-transfer degree, molecular charge-transfer solids can be insulators, semiconductors, metals and even superconductors.³ Molecular crystal engineering coincides with advances in our understanding of supramolecular chemistry and intermolecular non-covalent interactions, such as van der Waals, H-bonding and π - π stacking interactions.^{4–6} Interfacial and crystal engineering represents a paradigm for control over new solid phases with predictable architectures and geometries. The physicochemical properties of molecular crystalline solids are critically dependent on the molecular component distribution within the lattice and the properties of the individual constituent components. In this regard, crystallization engineering opens a door not only for the growth of new multifunctional materials but also for the exploration of novel physical and chemical phenomena.^{2,7,8} In

Rational design of molecular crystals for enhanced charge transfer properties†

Ying-Shi Guan,^a Zhuolei Zhang,^a Jinbo Pan,^b Qimin Yan^b and Shenqiang Ren^{id}*^a



Scheme 1 Chemical structures of donor and acceptor molecules.

addition, it should be noted that a controlled charge-transfer degree can be realized by integrating molecular electron acceptor with donor components with the electron affinity of the acceptor molecule in the ionization energy range of the electron donor. This has stimulated considerable research efforts in the design of such donor materials.^{9–13}

Here we report crystal engineering for the growth of molecular charge-transfer crystals, consisting of [1]benzothieno[3,2-*b*][1]benzothiophene (BTBT) based donors and a tetracyanoquinodimethane (TCNQ) based acceptor. Scheme 1 shows the chemical structures of BTBT based donor molecules and a TCNQ acceptor molecule. The choice of BTBT based donor molecules is motivated by their high charge carrier mobility, chemical stability and ease of derivatization,^{12,13} while TCNQ is a well-studied electron acceptor with high electron mobility.¹⁴ Furthermore, we employ two different crystal engineering strategies for the development of bilayer and crystal solid structures for the fundamental charge transfer processes.¹⁵ The resulting structures reveal striking differences in the fundamental charge-transfer processes for multifunctionality. While the intermolecular charge-transfer induces an increase in photoconductivity and pyroelectricity of BTBT:TCNQ solids, comparable responses do not occur for the bilayer microstructure. Our study suggests the exclusive formation of three-dimensional charge-transfer complexes with pronounced intermolecular hybridization in BTBT:TCNQ co-crystal solids.

Results and discussion

The charge-transfer complex is engineered in a bilayer arrangement, as shown in Fig. 1a, in view of the equally crystalline nature of *C_n*-BTBT (*n* = 0 or 10) and TCNQ. Single crystalline donor or

^a Department of Mechanical Engineering and Temple Materials Institute, Temple University, Philadelphia, PA 19122, USA. E-mail: shenqiang.ren@temple.edu

^b Department of Physics, Temple University, Philadelphia, PA 19122, USA

† Electronic supplementary information (ESI) available. See DOI: 10.1039/c7tc04316c

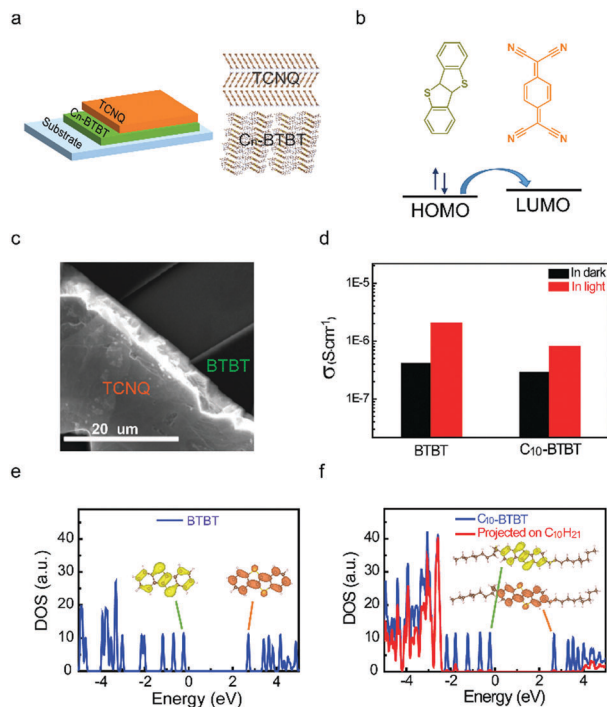


Fig. 1 (a) Schematic diagram of a donor–acceptor bilayer structure and the packing arrangement of the donor–acceptor bilayer where donor molecules and acceptor molecules are crystallized separately and laminated together. (b) Schematic diagram of electrons from the HOMO of the donor molecules transferring into the LUMO of the acceptor molecules. (c) The SEM image of a BTBT–TCNQ bilayer structure. (d) Conductivity and photoconductivity of bilayer structures with BTBT and C10–BTBT as the donor molecules. (e) Density of states and charge distribution of the HOMO and LUMO of a BTBT molecule. (f) Density of states and charge distribution of the HOMO and LUMO of a C10–BTBT molecule, and the red curve is the projected density of states on C₁₀H₂₁ chains.

acceptor layer structures can be grown on a water surface by controlling the rate of evaporation.¹⁶ Fig. 1a illustrates the bilayer geometry of donor and acceptor nanosheets, in which electrons in the highest occupied molecular orbital (HOMO) of BTBT are transferred to the lowest unoccupied molecular orbital (LUMO) of TCNQ. In such a bilayer geometry, the BTBT and TCNQ nanosheets behave as decoupled structures with virtually no hybridization between molecular levels, in which the positive and negative charges are separated into each layer. It can also be rationalized in terms of the heterostructure energy band diagram, accounting for the source of charge-transfer across the interface from the surface of the BTBT crystal to that of the TCNQ (Fig. 1b).

The scanning electron microscopy (SEM) images and the nitrogen and sulfur chemical analysis mapping from energy dispersive X-ray spectroscopy (EDS) reveal a bilayer structure (Fig. 1c and Fig. S1, ESI[†]). To determine the relative molecular orientation within the films, we solved the structures through X-ray diffraction (Fig. S2 and S3, ESI[†]). The bilayer samples showed a diffraction pattern which is a combination of C_n-BTBT (*n* = 0 or 10) and TCNQ patterns. The photoabsorption spectrum (Fig. S4, ESI[†]) of a BTBT–TCNQ bilayer shows a clear contribution of the BTBT and TCNQ absorption, implying the physical integration after two materials are brought into contact.

The same phenomenon has been observed in the C10–BTBT–TCNQ bilayer microstructures (Fig. S5, ESI[†]). The photoresponse properties of the BTBT and C10–BTBT donors have been analyzed on a bilayer heterojunction. We observe a decrease in conductivity (Fig. 1d) by extending a long alkyl side chain of BTBT derivatives. The large dark current in the BTBT–TCNQ bilayer suggests the alkyl side chain effect on the charge transport of heterojunctions. In the meantime, an increase of photocurrent under light illumination can be observed relative to the current in the dark in both bilayer structures. The BTBT–TCNQ bilayer structures exhibit higher current densities under light and dark conditions and higher photocurrent on/off ratios (Fig. S8, ESI[†]) than those of the C10–BTBT–TCNQ bilayer. The introduction of a long alkyl side chain in the BTBT donor structure produces a decrease of photoconductivity under AM1.5 solar illumination (Fig. 1d). This observation can be interpreted by the fact that the BTBT molecules have a stronger charge transfer interaction with TCNQ at the BTBT–TCNQ interface than that of the C10–BTBT molecules. The long alkyl side chain would lead to a weaker interfacial charge-transfer between the donor and acceptor. In other words, BTBT–TCNQ interfaces allow efficient charge-transfer interactions.^{1,17,18} To understand the difference in charge transfer at the BTBT–TCNQ and C10–BTBT–TCNQ interfaces, we carry out first-principles simulations of the electronic structures of BTBT and C10–BTBT molecules. The calculations are carried out using Kohn–Sham theory,¹⁹ projector augmented wave (PAW) potentials,²⁰ and the Perdew, Burke, and Ernzerhof (PBE) functional²¹ as implemented in the VASP code.²² We use an energy cutoff of 400 eV for the plane-wave basis set and a Γ -point-only *k* mesh for the integrations over the Brillouin zone. As shown in Fig. 1e and f, it is clear that the density of states of C10–BTBT in the energy window within 1 eV of the frontier orbitals (LUMO and HOMO) is almost identical to that of BTBT. The projected density of states of C₁₀H₂₁ chains (Fig. 1f) has no significant contribution to the total density of states in the energy window between 2 eV below the HOMO and 1 eV above the LUMO, which indicates that the electronic states of C₁₀H₂₁ chains are not involved in the carrier transport under a finite voltage. Instead, these chains behave as “insulation layers” between donor and acceptor states. This geometric effect is responsible for the decrease in charge transfer and the limited transport behavior at the C10–BTBT–TCNQ interface.

Considering the electron-donating ability of BTBT and the electron-accepting ability of TCNQ, highly single crystalline micro-tubes are synthesized as the mixed CT co-crystal due to the well-matched structural relationships between BTBT and TCNQ. The growth process is illustrated in Fig. 2a. The corresponding optical microscopy images reveal the growth processes of tubular structures of the BTBT:TCNQ complex through solution dissolution and recrystallization processes by dropping the TCNQ solution onto BTBT nanosheets. In brief, a droplet of TCNQ solution dissolved in acetonitrile is dropped onto the BTBT layer prepared *via* a solution epitaxy method. A dark precipitate appears immediately with the spreading of the TCNQ solution on the surface of BTBT. Scanning electron microscopy (SEM) images exhibit the formation of BTBT:TCNQ micro-tubes

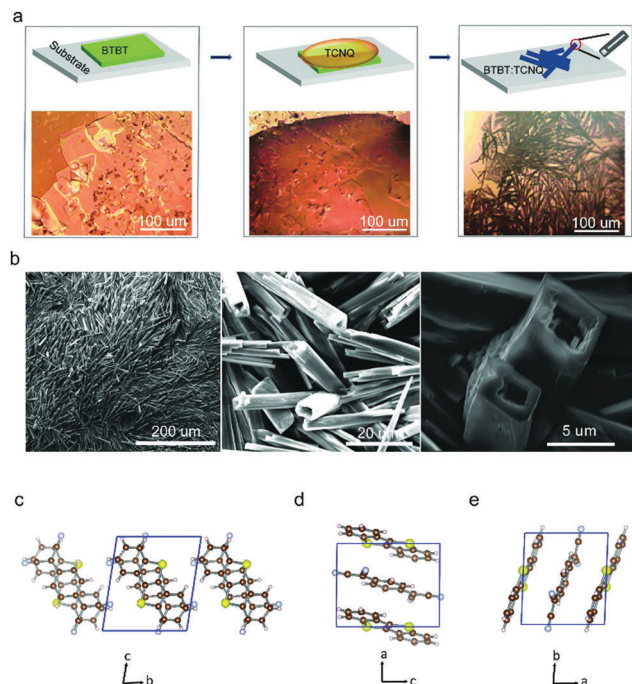


Fig. 2 (a) Schematic diagram illustrating the formation processes of BTBT:TCNQ tubes and the relative optical images of every stage. (b) SEM images of BTBT:TCNQ tubes at different magnifications. (c) Crystal structure of a BTBT:TCNQ co-crystal along the *a* axis. (d) Crystal structure of a BTBT:TCNQ co-crystal along the *b* axis. (e) Crystal structure of a BTBT:TCNQ co-crystal along the *c* axis.

(Fig. 2b), which reveal hollow tubular nanostructures with an average length of $\sim 150 \mu\text{m}$ and a wall thickness of $\sim 1.5 \mu\text{m}$. According to the above growth processes, a growth mechanism for 1D micro-tubes of the BTBT:TCNQ crystal is proposed.²³ While the BTBT layer has limited solubility in acetonitrile, the replacement of BTBT donor sites by TCNQ acceptor molecules should be favored by the stronger intermolecular charge transfer interactions to form molecular micro-tubular solids. With the spreading of the TCNQ solution, many small BTBT:TCNQ complexes as a unit further undergo a random aggregation and are prone to form hollow channels among themselves. Moreover, the XRD patterns in Fig. S6 (ESI[†]) reveal that the BTBT:TCNQ tubular solids have a single-crystalline structure. Meanwhile, the molecular packing configuration in the bulk crystal of BTBT:TCNQ (Fig. 2c–e) reveals that the donor and acceptor molecules are nearly planar and stack alternately along the *a*-axis, suggesting an intrinsic CT interaction between BTBT and TCNQ. The UV-Vis absorption spectrum (Fig. S7, ESI[†]) also confirms the strong CT interaction between BTBT and TCNQ, with a new absorption band appearing from 600 nm to 900 nm. High photoconductivity is observed for the BTBT:TCNQ tubular solids (Fig. S9, ESI[†]), while a light intensity dependent photoresponse results from the photogenerated charge carriers within the solids. The charge-transfer interactions between donor and acceptor molecules have a favorable effect on the charge transport and charge separation due to the efficient dissociation of photogenerated excitons.²⁴

We further explore the molecular crystal engineering effect on the mechanical strength of the charge-transfer bilayer and

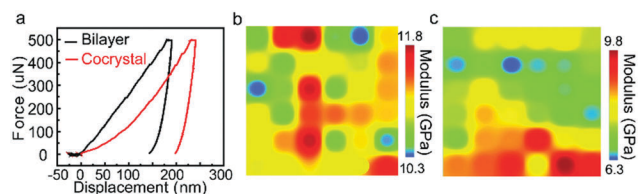


Fig. 3 (a) The displacement curves for BTBT–TCNQ bilayers and BTBT:TCNQ co-crystals. (b) Ultra-fast extreme property mapping (XPM) measurement for BTBT–TCNQ bilayers. (c) Ultra-fast extreme property mapping (XPM) measurement for BTBT:TCNQ co-crystals.

co-crystal structures through nanoindentation. Fig. 3a shows the compressive displacement curves for BTBT–TCNQ bilayers and BTBT:TCNQ co-crystals. The average Young's modulus of the BTBT:TCNQ co-crystals is 8.98 GPa, while the average Young's modulus of the BTBT–TCNQ bilayers is 11.04 GPa (Fig. 3b and c). The BTBT:TCNQ co-crystal shows a lower Young's modulus than that of the BTBT–TCNQ bilayer structure, due to the donor–acceptor CT complex formation through the replacement of BTBT donor sites by TCNQ acceptor molecules. In addition, the unique charge transfer and the exchange interaction between BTBT donors and TCNQ acceptors of the organic charge-transfer (CT) complexes give rise to a permanent dipole moment. The preferentially aligned dipoles result in a source of polarization in molecular tubular BTBT:TCNQ solids. The dipole induced pyroelectric properties of the BTBT:TCNQ micro-tubes are shown by periodic cooling and heating.^{25–27} The short-circuit currents of the BTBT:TCNQ crystals are measured by varying the temperature from 295 K to 307 K. As shown in Fig. 4a, a sharp negative current pulse ($\sim 11.2 \text{ pA}$) is observed when the temperature is increased from 295 K to 307 K, and the corresponding positive pulse is shown when the temperature is decreased to 295 K. Furthermore, when an external magnetic field is applied (Fig. 4b and Fig. S10 and S11, ESI[†]), the peak values of the pyroelectric current are consequently increased due to external magnetic field induced singlet to triplet conversion.²⁸ Fig. 4c presents the

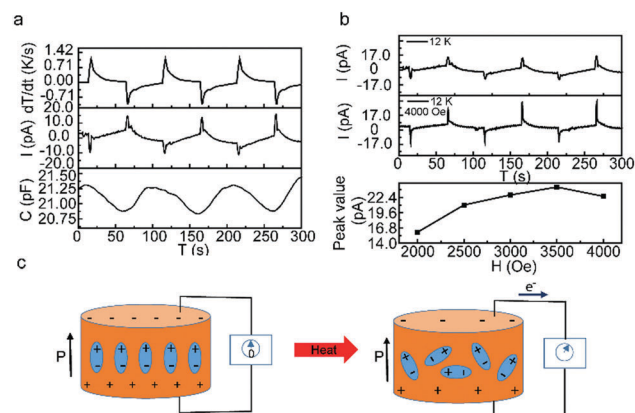


Fig. 4 (a) The cyclic changes in the temperature of a pyroelectric nano-generator and the corresponding differential curves, measured short-circuit current and capacitance upon increasing the temperature from 295 K to 307 K. (b) Measured short-circuit currents under different external magnetic fields. (c) Schematic illustration of the pyroelectric property generation mechanism in BTBT:TCNQ co-crystals.

pyroelectric property generation mechanism²⁹ of the BTBT:TCNQ crystals, while electric dipoles remain in the equilibrium state under the constant polarization of the BTBT:TCNQ crystals. When an external heat source is applied, the aligned electric dipoles oscillate, which would lead to the polarization change of BTBT:TCNQ crystals, resulting in the generation of pyroelectric current.

Conclusions

In conclusion, the fundamental charge-transfer processes are demonstrated by employing two different crystal engineering strategies for the development of bilayer and crystal solid structures. In the bilayer geometry, the length of the alkyl side chain between BTBT and C10-BTBT donors play an important role in the charge-transfer processes by combining with the TCNQ acceptor. When contrasting a three-dimensional co-crystal with the donor-acceptor bilayer structure, we observe three-dimensional co-crystal solids with unique mechano-pyro-electric coupling properties. The results shown here facilitate the understanding of the relationship between molecular stacking and functional properties in molecular charge-transfer solids.

Experimental

Fabrication of BTBT-TCNQ and C10-BTBT-TCNQ bilayer structures

We first prepared a 1 mg mL⁻¹ of BTBT, C10-BTBT and TCNQ with toluene in a 5 mL screw type vial and then dropped dozens of microliters of the solutions of the two BTBT derivatives (BTBT and C10-BTBT) and TCNQ onto a water surface respectively. The solution spread quickly over the whole water surface. Then we obtained their single crystalline micro-plate on the water surface by controlling the rate of evaporation. The obtained single crystalline micro-plate was easily transferred to any substrate such as glass or silicon. We first transferred a donor molecule layer onto the substrate and then transferred an acceptor molecule layer on the surface of the donor molecule layer to obtain a donor-acceptor bilayer structure.

Fabrication of BTBT:TCNQ co-crystal tubes

Firstly, we prepared a 5 mg mL⁻¹ (final concentration) of TCNQ with acetonitrile in a 5 mL screw type vial and then dropped dozens of microliters of the TCNQ solution onto the surface of the BTBT single crystalline micro-plate prepared through the method mentioned above. A dark precipitate appeared immediately with the spreading of the TCNQ solution on the surface of BTBT.

Fabrication of bilayer structure and micro-tube devices

For the preparation of bilayer samples, patterned ITO substrates were sonicated continuously in soap water, distilled water, acetone and isopropyl alcohol for 10 min and then blown dry with N₂. The substrates were then irradiated with oxygen plasma for 10 min. TFB was spun-coated on the substrates at a speed of 3500 rpm for 1 min and dried at 100 °C for 30 min. The fabricated donor layers were transferred onto the substrates.

The devices were allowed to stay overnight, and then the acceptor layer was transferred onto the substrates. Then the devices were dried at 80 °C for 120 min in a glovebox. A 3.5 nm bathocuproine layer was deposited by thermal evaporation, followed by the deposition of 100 nm aluminum electrodes.

For the preparation of micro-tube samples, patterned ITO substrates were sonicated continuously in soap water, distilled water, acetone and isopropyl alcohol for 10 min and then blown dry with N₂. The substrates were then irradiated with oxygen plasma for 10 min. TFB was spun-coated on the substrates at a speed of 3500 rpm for 1 min and dried at 100 °C for 30 min. The fabricated BTBT donor layers were transferred onto the substrates. The devices were allowed to stay overnight and then a droplet of solution of TCNQ dissolved in acetonitrile was dropped onto the BTBT layer. Then the devices were dried at 100 °C for 60 min in a glovebox. A 3.5 nm bathocuproine layer was deposited by thermal evaporation, followed by the deposition of 100 nm aluminum electrodes.

Characterization

The SEM images were taken from an FEI Quanta450FEG. UV-Vis spectra were recorded on an Agilent Model HP8453 UV-Vis spectrophotometer. The magnetic-field, light dependent current and current-voltage (*I-V*) characteristics of the devices are measured under atmospheric conditions with a CHI 422 Series Electrochemical Workstation with or without an applied magnetic field, or an illumination from an OSL2 fiber illuminator calibrated using a Newport Power Meter with Model 1918-R. A Bruker Apex II Duo single-crystal X-ray diffractometer was used to obtain the XRD pattern at a step of 0.3° per minute from 3° to 30°. Their mechanical properties were investigated on a TI 980 Triboindenter System.

Conflicts of interest

There are no conflicts of interest to declare.

Acknowledgements

Work at Temple University (S.R.) was supported by the Army Research Office Young Investigator Program (W911NF-15-1-0610). Mrs Audrey Richard and Prof. Yves Henri Geerts at the Université Libre de Bruxelles (ULB) for providing the donor molecules of this study are gratefully acknowledged. This research used resources of the National Energy Research Scientific Computing Center, a DOE Office of Science User Facility supported by the Office of Science of the U.S. Department of Energy under Contract No. DE-AC0205CH11231.

References

- 1 S. Prasanthkumar, S. Ghosh, V. C. Nair, A. Saeki, S. Seki and A. Ajayaghosh, *Angew. Chem., Int. Ed.*, 2015, **54**, 946–950.
- 2 W. Zhu, R. Zheng, X. Fu, H. Fu, Q. Shi, Y. Zhen, H. Dong and W. Hu, *Angew. Chem., Int. Ed.*, 2015, **54**, 6785–6789.

- 3 H. Alves, A. S. Molinari, H. Xie and A. F. Morpurgo, *Nat. Mater.*, 2008, **7**, 574–580.
- 4 A. S. Tayi, A. Kaeser, M. Matsumoto, T. Aida and S. I. Stupp, *Nat. Chem.*, 2015, **7**, 281–294.
- 5 K.-T. Wong and D. M. Bassani, *NPG Asia Mater.*, 2014, **6**, e116.
- 6 C. Sutton, C. Risko and J.-L. Brédas, *Chem. Mater.*, 2016, **28**, 3–16.
- 7 Y.-Q. Sun, Y.-L. Lei, X.-H. Sun, S.-T. Lee and L.-S. Liao, *Chem. Mater.*, 2015, **27**, 1157–1163.
- 8 A. Jain and S. J. George, *Mater. Today*, 2015, **18**, 206–214.
- 9 Y.-S. Guan, Y. Qin, Y. Sun, C. Wang, W. Xu and D. Zhu, *Chem. Commun.*, 2015, **51**, 12182–12184.
- 10 K. Takimiya, I. Osaka, T. Mori and M. Nakano, *Acc. Chem. Res.*, 2014, **47**, 1493–1502.
- 11 G. Schweicher, V. Lemaury, C. Niebel, C. Ruzié, Y. Diao, O. Goto, W. Y. Lee, Y. Kim, J. B. Arlin, J. Karpinska, A. R. Kennedy, S. R. Parkin, Y. Olivier, S. C. Mannsfeld, J. Cornil, Y. H. Geerts and Z. Bao, *Adv. Mater.*, 2015, **27**, 3066–3072.
- 12 C. Niebel, Y. Kim, C. Ruzié, J. Karpinska, B. Chattopadhyay, G. Schweicher, A. Richard, V. Lemaury, Y. Olivier, J. Cornil, A. R. Kennedy, Y. Diao, W.-Y. Lee, S. Mannsfeld, Z. Bao and Y. H. Geerts, *J. Mater. Chem. C*, 2015, **3**, 674–685.
- 13 Y. Tsutsui, G. Schweicher, B. Chattopadhyay, T. Sakurai, J.-B. Arlin, C. Ruzié, A. Aliev, A. Ciesielski, S. Colella, A. R. Kennedy, V. Lemaury, Y. Olivier, R. Hadji, L. Sanguinet, F. Castet, S. Osella, D. Dudenko, D. Beljonne, J. Cornil, P. Samori, S. Seki and Y. H. Geerts, *Adv. Mater.*, 2016, **28**, 7106–7114.
- 14 Y. Krupskaya, M. Gibertini, N. Marzari and A. F. Morpurgo, *Adv. Mater.*, 2015, **27**, 2453–2458.
- 15 H. Mendez, G. Heimel, A. Opitz, K. Sauer, P. Barkowski, M. Oehzelt, J. Soeda, T. Okamoto, J. Takeya, J. B. Arlin, J. Y. Balandier, Y. Geerts, N. Koch and I. Salzmann, *Angew. Chem., Int. Ed.*, 2013, **52**, 7751–7755.
- 16 C. Xu, P. He, J. Liu, A. Cui, H. Dong, Y. Zhen, W. Chen and W. Hu, *Angew. Chem., Int. Ed.*, 2016, **55**, 9519–9523.
- 17 H. Huang, D. E. Gross, X. Yang, J. S. Moore and L. Zang, *ACS Appl. Mater. Interfaces*, 2013, **5**, 7704.
- 18 Y.-S. Guan, Y. Qin, Y. Sun, J. Chen, W. Xu and D. Zhu, *Chem. Commun.*, 2016, **52**, 4648–4651.
- 19 W. Kohn and L. J. Sham, *Phys. Rev.*, 1965, **140**, A1133–A1138.
- 20 P. E. Blochl, *Phys. Rev. B: Condens. Matter Mater. Phys.*, 1994, **50**, 17953–17979.
- 21 J. P. Perdew, K. Burke and M. Ernzerhof, *Phys. Rev. Lett.*, 1996, **77**, 3865–3868.
- 22 G. Kresse and J. Furthmüller, *J. Comput. Mater. Sci.*, 1996, **6**, 15–50.
- 23 X. Fang, X. Yang and D. Yan, *J. Mater. Chem. C*, 2017, **5**, 1632–1637.
- 24 H. Huang, C. E. Chou, Y. Che, L. Li, C. Wang, X. Yang, Z. Peng and L. Zang, *J. Am. Chem. Soc.*, 2013, **135**, 16490–16496.
- 25 C. R. Bowen, J. Taylor, E. LeBoulbar, D. Zabeck, A. Chauhan and R. Vaish, *Energy Environ. Sci.*, 2014, **7**, 3836–3856.
- 26 A. N. Morozovska, E. A. Eliseev, G. S. Svechnikov and S. V. Kalinin, *J. Appl. Phys.*, 2010, **108**, 042009.
- 27 Y. Yang, W. Guo, K. C. Pradel, G. Zhu, Y. Zhou, Y. Zhang, Y. Hu, L. Lin and Z. L. Wang, *Nano Lett.*, 2012, **12**, 2833–2838.
- 28 W. Qin, M. Gong, T. Shastri, M. C. Hersam and S. Ren, *Sci. Rep.*, 2014, **4**, 6126.
- 29 D. Zabeck, J. Taylor, E. L. Boulbar and C. R. Bowen, *Adv. Energy Mater.*, 2015, **5**, 1401891.